

Charge and spin properties of a generalized Wigner crystal realized in the moiré WSe₂/WS₂ heterobilayer

Andrzej Biborski^{1,*} and Michał Zegrodnik^{1,†}

¹*Academic Centre for Materials and Nanotechnology,
AGH University of Krakow, Al. Mickiewicza 30, 30-059 Krakow, Poland*

We examine the charge and spin properties of an effective single-band model representing a moiré superlattice of the WSe₂/WS₂ heterobilayer. We focus on the 2/3 electron filling, which refers to the formation of a generalized Wigner crystal, as evidenced experimentally. Our approach is based on the extended-Hubbard model on a triangular lattice with non-interacting part effectively describing a spin-split band due to Ising-type spin-orbit coupling. We investigate the system in the regime of strong on-site Coulomb repulsion and the ground state of the Hamiltonian is obtained with the use of the Density Matrix Renormalization Group formulated within the Matrix Product State approach. According to our analysis, based on the density-density correlation functions resolved in the momentum space, a transition from the metallic to the insulating state appears with increasing intersite electron-electron interactions. This transition is identified as being concomitant with the emergence of a generalized Wigner crystal that realizes the honeycomb lattice pattern. We investigate the magnetic properties of such a Wigner crystal state and find that the presence of spin-valley polarization and the increased intersite repulsion induce spin canting of the out-of-plane antiferromagnetic ordering.

I. INTRODUCTION

Strong electronic correlations in fermionic systems are believed to be the origin of a number of exotic phenomena that cannot be understood with the help of single-particle or mean-field theories. The widely known examples of such effects are: the formation of the insulating gap induced by local Coulomb repulsion which is the essence of the Mott-Hubbard transition^{1,2}, variety of spin- or charge-ordered phases¹, as well as the pairing mechanism resulting in unconventional superconductivity^{3,4}.

The role of electron-electron interactions in many particle systems is not limited to typical condensed matter systems, i.e. to those where electronic degrees of freedom are coupled to the underlying ionic lattice structure. In fact, the formation of a Wigner crystal⁵ (WC) in the electron gas can be considered a canonical example of correlation-induced effects when interactions between electrons predominate the kinetic energy contribution at the properly selected particle concentration⁶. The idea of WC formation is almost one hundred years old⁶. Over the years the pursuit for its experimental realization has motivated the study of 2D systems in the presence of relatively high magnetic fields, which suppress the contribution resulting from the kinetic energy due to the formation of Landau levels. Very recently, a direct visualization of WC by high-resolution scanning microscopy has allowed identification of its symmetry and melting in Bernal-stacked bilayer graphene⁷. The recent discovery of flat bands in moiré transition metal dichalcogenide bilayers, in particular WSe₂/WS₂ heterobilayer, has opened a new route for the realization of WC without the need to apply a magnetic field^{8–12}. In fact, in such system the obtained pattern of localized charges should be considered as a generalized Wigner (GWC) crystal, since it is realized in an environment created by the un-

derlying crystal lattice. At selected fractional fillings of the WSe₂/WS₂ flat band, a GWC state can be created that may be considered as a *extreme* form of charge density wave (CDW) induced by the non-local (intersite) Coulomb interactions. In such a scenario, only certain sublattices of the moiré superlattice are occupied and a gap opens as suggested by the experiments^{9,10}.

It is believed that the moiré flat band of WSe₂/WS₂ can be described using an effective single band model on a triangular lattice with spin-valley locking incorporated with the use of the spin-dependent complex phase of the hoppings¹³. By supplementing such an approach with the electron-electron interaction terms, one obtains the Hubbard-like description¹⁴. Along these lines the formation of the GWC realizing a Kagome pattern at $n = 3/4$ filling, as well as its magnetic properties have been analyzed in the strong coupling limit when the hopping processes are completely suppressed leading to a Heisenberg model supplemented with the Dzyaloshinskii-Moriya term¹⁵. Also, interesting studies of the physics of GWC formation on a triangular lattice with the use of extended Hubbard and continuum models have also been reported in Refs. 14, 16–18, however without the inclusion of spin-valley locking.

Here, we focus on analyzing the charge pattern formation leading to the GWC as well as its magnetic properties at selected fractional filling ($n = \frac{2}{3}$) by taking into account both the strong electron correlation effects induced by long-range Coulomb interactions and the spin-valley locking, at the same time. We start from establishing the model and briefly present the applied computational method, which is the Density Matrix Renormalization Group (DMRG) in the Matrix Product State (MPS) formulation. The DMRG method is considered to be one of the *state of art* approaches for interacting fermionic systems. Next, we present both charge and spin properties by investigating one- and two-particle correlation

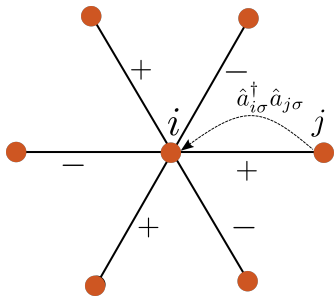


FIG. 1. Schematic representation of the sign of phase ϕ_{ij} from Eq. 1. The dashed arrow represents exemplary hopping process which is weighted by factor $|t|e^{i\tilde{\sigma}\phi_{ij}}$.

functions. Treating the nearest-neighbor (nn) intersite Coloumb interaction V as a free parameter, we demonstrate the indicators that reveal the transition from the metallic state to the insulating state for which the GWC emerges concomitantly with increasing V . Also, by inspecting the spin-spin correlation function we provide evidence of coexisting canted antiferromagnetism for the values of V , which recovers experimental findings. To the best of our knowledge, this kind of analysis is performed for the first time. We conclude our findings in the last Section of the paper.

II. MODEL AND METHOD

The single particle part of the Hamiltonian effectively describing spin-split flat moiré band of WSe₂/WS₂ is given as¹³

$$\hat{\mathcal{H}}_0 = \sum_{\langle i,j \rangle} \sum_{\sigma} |t| e^{i\tilde{\sigma}\phi_{ij}} \hat{a}_{i,\sigma}^{\dagger} \hat{a}_{j,\sigma}, \quad (1)$$

where $\hat{a}_{i,\sigma}^{\dagger}$ ($\hat{a}_{i,\sigma}$) are standard fermionic operators creating (annihilating) electrons with spin z-component $\sigma = \{\uparrow, \downarrow\}$ at lattice site i . The spin dependant complex hoppings in $\hat{\mathcal{H}}_0$ incorporate the Ising type spin-orbit coupling which appears in the considered system and result in a spin-valley locking. In our notation $\tilde{\sigma} = 1(-1)$ for $\sigma = \uparrow(\downarrow)$ and $\phi_{ij} = \pm \frac{2}{3}\pi$ with the sign convention depicted in Fig. 1. The interacting part of the Hamiltonian is taken as

$$\hat{\mathcal{H}}_{e-e} = \sum_i U \hat{n}_{i\uparrow} \hat{n}_{i\downarrow} + \frac{1}{2} \sum_{\langle ij \rangle} V \hat{n}_i \hat{n}_j, \quad (2)$$

where $\hat{n}_{i\sigma} \equiv \hat{a}_{i\sigma}^{\dagger} \hat{a}_{i\sigma}$ and $\hat{n}_i \equiv \hat{n}_{i\uparrow} + \hat{n}_{i\downarrow}$. The first and the second term in Eq. (2) describes the onsite and nearest neighbor (nn) intersite Coulomb repulsion, respectively. The resulting model consists of both (1) and (2) terms ,

$$\hat{\mathcal{H}} = \hat{\mathcal{H}}_0 + \hat{\mathcal{H}}_{e-e}, \quad (3)$$

and represents an extended Hubbard model (EH) on a triangular lattice with spin-valley locking. To characterize the approximate many-particle ground state $|\Psi\rangle$

of Hamiltonian (3) we employ finite DMRG¹⁹ approach in MPS formulation^{20,21} using ITensor library²². In this variant, both the *ansatze* of $|\Psi\rangle$ and the Hamiltonian at hand are given by products of matrices in such manner that the DMRG sweeping procedure can be efficiently implemented taking advantage of the tensorial nature of these representations of states and operators²⁰. The resulting MPS for the system consisting of the N lattice sites is given as²⁰

$$|\Psi\rangle = \sum_{\substack{\delta_1, \dots, \delta_N \\ \alpha_1, \dots, \alpha_{N-1}}} A_{\delta_1}^{\alpha_1 \alpha_0} A_{\delta_2}^{\alpha_2 \alpha_1} \dots A_{\delta_N}^{\alpha_N \alpha_{N-1}} |\delta_1, \delta_2, \dots, \delta_N\rangle, \quad (4)$$

where $\{\delta_i\}$ refer to physical degrees of freedom at i -th lattice site and entries of matrices $A_{\delta_i}^{\alpha_i \alpha_{i-1}}$ are to be determined. Although MPS can be considered as the natural way to describe the ground state of one-dimensional Hamiltonians, it can also be adapted to the two-dimensional (2D) cases. To achieve this, we apply the ordering of lattice sites (see Fig. 2a) to emulate the 2D system with the vectors $\mathbf{R}_1 = (1, 0)$ and $\mathbf{R}_2 = \frac{1}{2}(-1, \sqrt{3})$. In addition, we impose the periodic boundary conditions along the \mathbf{R}_2 direction and open boundary conditions in the \mathbf{R}_1 direction as presented in Fig. 2(b). The Hamiltonian represented by the matrix product operator (MPO) has complex-valued entries (as well as the MPS). Therefore, the operations during DMRG sweeps are more demanding than in the real-valued case. Eventually, the considered supercell with the boundary conditions imposed refers to the cylinder, which is a standard approach to investigate 2D systems in the framework of DMRG methods²³⁻²⁵.

III. RESULTS

All calculations discussed here correspond to $|t| = 1$ and $U = 15|t|$ representing a strongly correlated scenario that is believed to be realized in WSe₂/WS₂ heterobilayer. For this system $U/|t| \approx 15$ and $V/|t| \approx 5$ [14], the moiré band width is $W \approx 9|t|$. However, we extend our analysis to $V \in (0, 6|t|)$ in order to study the gradual formation of the GWC through a precursor CDW state as the strength of the intersite Coulomb term is increased. We set $L_1 = 24$ and $L_2 = 6$ in the cylindrical system, since the order of the emerging lattice structure of the GWC (for significant values of V) is expected to be commensurate^{14,26} with the period $\Delta L_{1,2} = 3$ for band filling $n = N_e/N = \frac{2}{3}$, where $N = L_1 \times L_2$, and, N_e is a number of carriers considered. In addition to imposing a constant number of particles, we also assume a total z-spin component $S_{tot}^z = \sum_i \langle \hat{S}_i^z \rangle = 0$ (see the appendix for more details). All calculations have been performed for the maximal link dimensions [α_i in Eq. (4)] up to 8192, resulting in a truncation error lower than 10^{-4} for all the cases considered.

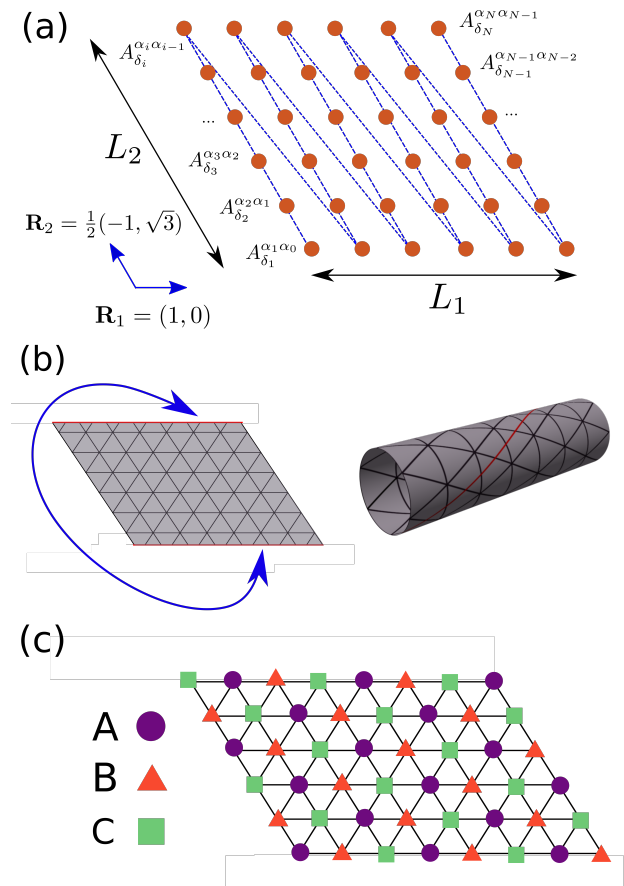


FIG. 2. (a) The sketch of MPS where the chosen ordering of A matrices related to a given lattice sites is optimal for providing periodic boundary conditions along \mathbf{R}_2 vector. The total number of lattice sites is $N = L_1 \times L_2$ where L_1 and L_2 are numbers of unit cells in directions given by \mathbf{R}_1 and \mathbf{R}_2 , respectively. (b) The periodic boundary conditions are provided along \mathbf{R}_2 . The red lines in 2D lattice supercell are *glued* together creating a cylinder shape provided in the Figure. (c) The triangular lattice can be divided into three triangular sublattices which are labeled by A , B and C .

A. Charge order and gap

We first determine the influence of the term V on the spatial distribution of the charge over the moiré lattice sites. In Fig. 3, we present $\langle \hat{n}_{i(x,y)} \rangle$ for the representative values of V . The complete set of data collected for various values V is available in an online repository²⁷. As can be seen, the electron distribution is almost homogeneous (disregarding minor edge effects) for $V = 0$ [Fig. 3(a)], whereas with increasing V the CDW develops [Fig. 3(b)]. Subsequently, for $V \gtrsim 3|t|$ a clear honeycomb pattern of occupied lattice sites can be observed with all remaining sites, forming a triangular sublattice, being empty, as shown in Fig. 3(c). For even stronger intersite Coulomb strength, when $V \approx 6.0|t|$, a reversed situation occurs with a triangular sublattice occupied (Fig. 3 d) and a honeycomb sublattice empty. This behavior is in agree-

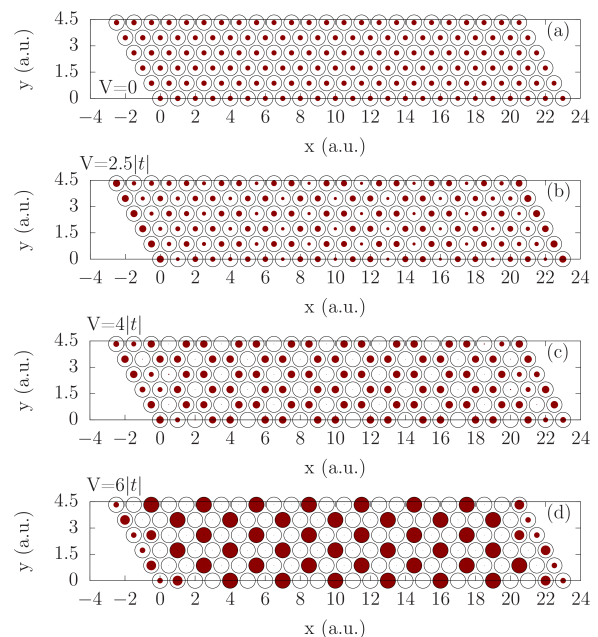


FIG. 3. Spatial charge distribution in 24×6 cylinder for the three representative values of V . The hollow circles represent the lattice sites. The diameter of the filled red circles is proportional to $\langle \hat{n}_{i(x,y)} \rangle$. The completely filled circles represent doubly occupied sites.

ment with the one corresponding to the case of EH in a triangular lattice obtained without the inclusion of spin-valley locking²⁶. Following Tocchio et al.²⁶ we employ the nomenclature with respect to the three recognized types of order, e.g. $(\frac{2}{3} \frac{2}{3} \frac{2}{3})$, (110) and (200) referring to the situation where carriers occupy three, two and one triangular sublattice (-s), each labeled by $\alpha \in \{A, B, C\}$ (see Fig.2c).

In Fig. 4 we present our results in a more quantitative way, that is, we plot the electron occupation at subsequent lattice sites along the direction \mathbf{R}_1 at $y = 0$. As can be seen, the finite size of the system and the open boundary conditions in the \mathbf{R}_1 direction only slightly affect the densities close to the edges of the supercell. Furthermore, it is clearly visible in Fig. 4(a) that for $V = 0$ the charges are uniformly distributed with $\langle \hat{n}_{i(x,0)} \rangle \approx 2/3$. Again, as shown in Fig. 4(b), for $V = 2.5|t|$ we observe a CDW modulation with the three triangular sublattices referring to $(\frac{1}{2} \frac{3}{4} \frac{3}{4})$. For $V = 4.0|t|$, the two sublattices are almost completely occupied and the remaining third sublattice has only residual occupancy [Fig.4(c)]. Finally, for $V = 6.0|t|$ the intersite repulsion overcomes the competitive Hubbard on-site interactions, and double occupancies are created on a single sublattice leaving the remaining two empty [Fig.4(d)].

For the sake of completeness in Fig. 5 we show the gradual evolution of the charge pattern induced by the presence of intersite Coulomb repulsion by plotting the average density $n_\alpha \equiv \frac{1}{3N} \sum_{i(\alpha)} \langle \hat{n}_{i(\alpha)} \rangle$ on each sublattice

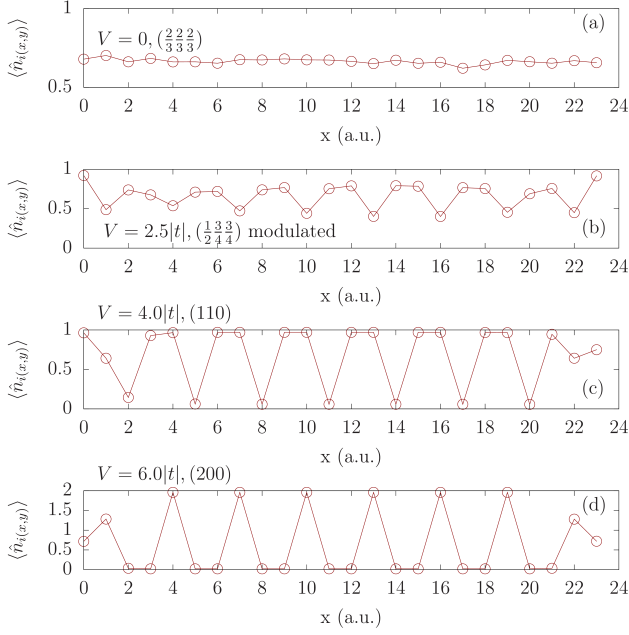


FIG. 4. Value of $\langle \hat{n}_{i(x,y=0)} \rangle$ for the 24×6 system for the representative values of V . Excluding the situation $V = 0$ (a), the modulation by a period of $\Delta L = 3$ is clearly visible.

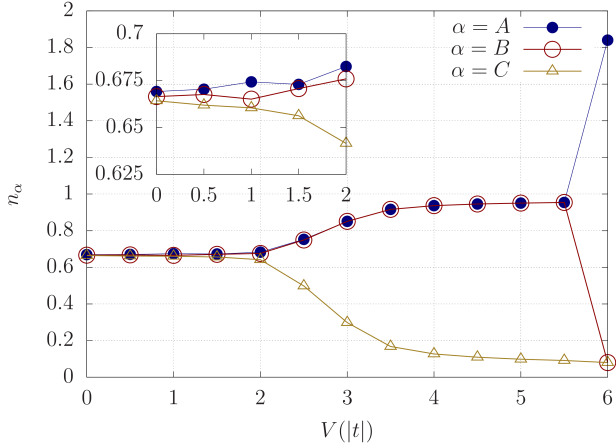


FIG. 5. The electron occupation n_α (see the main text) of the three sublattices A , B , and C as a function of intersite interaction V for the system of size 24×6 .

as a function of V . The differences between the three sublattices are rather weak for $V \lesssim 1.5|t|$ (see the inset in Fig.5). However, for $V \gtrsim 1.5|t|$, a precursor charge ordering appears and becomes more pronounced to finally achieve a nearly pure (110) pattern for $V \approx 4|t|$. This order is persistent up to $V \approx 5.5|t|$, where an abrupt redistribution of charges leads to the emergence of the (200) phase. Note that the emergence of the (110) order takes place for $U/V \approx 5$ and (200) becomes stable for $U/V \approx 3$.

Subsequently, we investigate the momentum space-

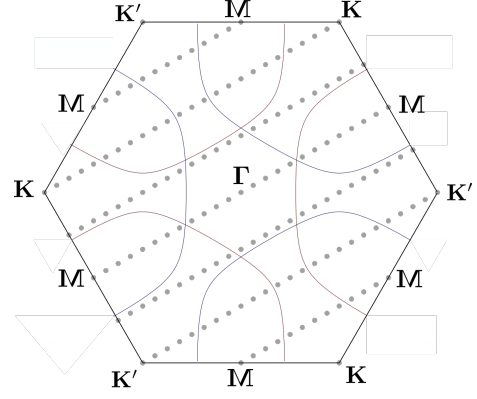


FIG. 6. Fermi surfaces (solid lines) obtained by diagonalization of the non-interacting part of Hamiltonian (i.e. for $\hat{\mathcal{H}}_0$) at filling $n = 2/3$. The solid red (blue) lines refer to the Fermi level of $\sigma = \uparrow$ (\downarrow) spin-valley split bands. The gray circles represent \mathbf{q} vectors available for the finite cylinder of size 24×6 , that is the largest considered in the DMRG approach.

resolved single-particle correlation functions defined as

$$n_{\mathbf{q}\sigma} = \frac{1}{N} \sum_{i,j} e^{i\mathbf{q}\cdot(\mathbf{r}_i - \mathbf{r}_j)} \langle \hat{c}_{i\sigma}^\dagger \hat{c}_{j\sigma} \rangle, \quad (5)$$

where $\{\mathbf{r}_i\}$ are vectors pointing to the lattice sites and \mathbf{q} are the momentum vectors. In Fig. 6 we present the available \mathbf{q} -space vectors for the cylinder of size 24×6 , as well as the Fermi surfaces for both spin-split bands resulting from the diagonalization of $\hat{\mathcal{H}}_0$ in the reciprocal space at $n = 2/3$. As one can see, in the non-interacting picture, Fermi surfaces are opened around \mathbf{K} and \mathbf{K}' points for $\delta = \uparrow$ and $\delta = \downarrow$ quasiparticles, respectively. The presence of C_3 symmetry for both spin subbands separately is an expression of the SOC encapsulated in $\hat{\mathcal{H}}_0$ that breaks the C_6 symmetry of the triangular lattice and results in the appearance of spin-valley locking¹⁴. The analysis of $n_{\mathbf{q}\sigma}$ may provide useful information with respect to the quasiparticles *dressed* in interactions²⁸. That is, the quasiparticle weight $Z_{\mathbf{q}}$ that measures the coherence in the fermionic interacting system²⁸ may serve as an indicator of the electron correlation strength. In Figs. 7(a-d) we show $n_{\mathbf{q}\sigma}$ along the $\Gamma - M - K - \Gamma$ path for the four representative values of V . Note that along the $\Gamma - M - K' - \Gamma$ trajectory the result is identical when one exchanges spin-up with spin-down quasiparticles. As one can see in Fig. 7(a), even for $V = 0$, the quasiparticles are renormalized due to the high value of U , since we do not observe an abrupt decrease in $n_{\mathbf{q}\sigma}$ for $\mathbf{q} \in M - \Gamma$ in the vicinity of the point where the two branches of Fermi surfaces cross (see Fig.6). The similar observation holds for $V = 2.5|t|, 4.0|t|$ and $6.0|t|$ as shown in Figs. 7(b-d). Although the $\mathbf{K} - \mathbf{M}$ section is affected by a lower density of \mathbf{q} points, an abrupt decrease in $n_{\mathbf{q}\uparrow} (n_{\mathbf{q}\downarrow})$ seems to appear at $\mathbf{q}_{K-M} \equiv (\mathbf{K} - \mathbf{M})/2$. Apparently, at \mathbf{q}_{K-M} , the occupancy, $n_{\mathbf{q}}$, is higher by a value of ≈ 0.4 compared to

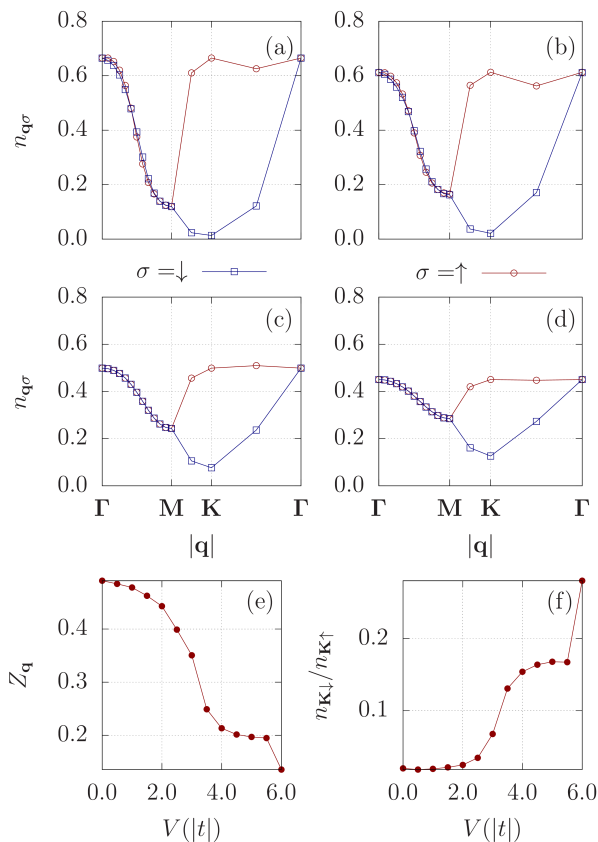


FIG. 7. Momentum resolved occupation number as a function of \mathbf{q} along the high symmetry directions in the reciprocal space for the four different values of V : (a) $V = 0$; (b) $V = 2.5|t|$; (c) $V = 4.0|t|$ and (d) $V = 6.0|t|$. The estimated value of $Z_{\mathbf{q}}$ (e), and the ratio $n_{\mathbf{K}\downarrow}/n_{\mathbf{K}\uparrow}$ (f), both as a function of V .

$\mathbf{q} = \mathbf{M}$. For $\sigma = \downarrow$, it concomitantly decreases to ~ 0.0 for $V = 0$, while for the higher values of intersite repulsions, the corresponding values become higher with increasing V . This, together with the general *flattening* of $n_{\mathbf{q}\sigma}$, signals further renormalization of quasiparticles driven by the increase of V . For $\mathbf{q} \in \Gamma - \mathbf{K}$, it can be deduced from Figs. 7(a-d) that $n_{\mathbf{q}\uparrow}$ remains nearly constant, while $n_{\mathbf{q}\downarrow}$ rapidly increases when the Fermi surface is crossed. Subsequently, the latter attains the same value as for spin-up carriers, as expected.

In Fig. 7(e) we show the estimated value of the quasi-particle weight given by $Z_{\mathbf{q}} \approx n_{\mathbf{q}_{\mathbf{K}-\mathbf{M}}} - n_{\mathbf{M}\sigma}$ as a function of V . For values $V \lesssim 3|t|$, the intersite interactions moderately modify $n_{\mathbf{q}\sigma}$ compared to the $V = 0$ case. When approaching $V \approx 3|t|$, the renormalization is significantly enhanced. For $3.5|t| \lesssim V \lesssim 5.5|t|$ no spectacular change can be observed in $Z_{\mathbf{q}}$, however, for $V = 6|t|$ an abrupt decrease associated with the formation of the (200)-ordered phase appears, indicating an extreme reorganization of the occupation scheme in the momentum space. The role of inter-site repulsion on spin-valley po-

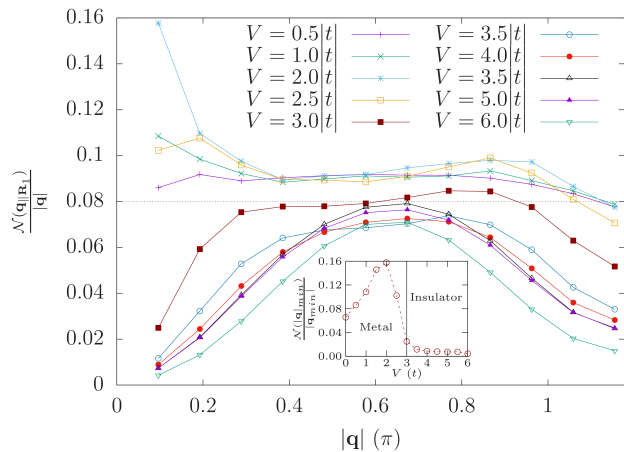


FIG. 8. The $\mathcal{N}(\mathbf{q})/|\mathbf{q}|$ dependence for selected values of V . The horizontal line at 0.08 roughly divides the curves referring to the metallic state from those showing insulating behavior (although the case $V = 0$ is an isolated exception to this rule). The inset shows the same quantity as the Figure itself, but for the smallest available \mathbf{q} as function of V .

larization can also be identified by inspecting the ratio $n_{\mathbf{K}\uparrow}/n_{\mathbf{K}\downarrow}$ as presented in Fig.7g. That is, interactions-driven *smearing* of Fermi surfaces result in decreased $n_{\mathbf{K}\uparrow}$ accompanied by increased occupation of \mathbf{K} momentum state by $\sigma = \uparrow$ quasiparticles. This behavior illustrates the reduction of anisotropy with respect to spin quantum number along the path $\mathbf{M} - \mathbf{K} - \Gamma$ in the single-particle occupation scheme with an increasing value of V .

To further characterize the electronic properties of the system in view of possible insulating gap opening due to long-range Coulomb repulsion, we investigate the Fourier transform of the two-body density-density correlation functions expressed as

$$\mathcal{N}(\mathbf{q}) = \frac{1}{N} \sum_{ij} e^{i\mathbf{q}\cdot(\mathbf{r}_i - \mathbf{r}_j)} \langle \hat{n}_i \hat{n}_j \rangle. \quad (6)$$

That is, $\lim_{|\mathbf{q}| \rightarrow 0} \mathbf{q}^2/\mathcal{N}(\mathbf{q})$ is proportional to the magnitude of the gap^{26,29-32}. According to the finite size of the system, it is convenient to inspect $\mathcal{N}(\mathbf{q})/|\mathbf{q}|$ for the smallest available value of $|\mathbf{q}|$. In fact, when $\mathcal{N}(\mathbf{q}) \sim |\mathbf{q}|^2$ for $|\mathbf{q}| \rightarrow 0$ it indicates the opening of the gap³¹. Although our approach breaks the translational symmetry due to the application of open boundary conditions in one direction, we find that the length of the cylinder considered here (i.e. $L_1 = 24$) is large enough to observe, at least qualitatively, an abrupt change in the character of $\mathcal{N}(\mathbf{q})/|\mathbf{q}|$ with increasing value of V .

In Fig. 8, we plot this quantity for \mathbf{q} along $\Gamma - \mathbf{M}$. Although the dependencies obtained for $V \lesssim 3|t|$ in the vicinity of $|\mathbf{q}| \rightarrow 0$ do not expose a regular pattern with increasing value of V they are clearly distinguishable from those obtained for $V \gtrsim 3|t|$. That is, for the latter case the values of $\mathcal{N}(\mathbf{q})/|\mathbf{q}|$ tend to zero monotonically when $|\mathbf{q}|$ decreases. This trend can also be seen in the

inset of Fig. 8 where we plot the same quantity as in the main figure (as a function of V) but only for the smallest value of $|\mathbf{q}|$ available in our calculations. Eventually, this analysis leads to the conclusion that the gap opens when $V \gtrsim U/5$. Note that this transition from metallic to insulating state is concomitant with the formation of a (110) charge pattern. Therefore, we conclude that also at $V \approx 5|t| = U/3$, e.g., which is believed to correspond to the WSe₂/WS₂ bilayer¹⁴, our results recover the experimental evidence showing the formation of the insulating GWC.

B. Spin order

The analysis of the charge distribution carried out in the previous subsection allows us to state that the considered model reconstructs the experimental situation from the point of view of the GWC appearance in the WSe₂/WS₂ heterobilayer. In this subsection, we characterize the spin properties of the system focusing mainly on (110) GWC case. Our analysis is based on the spin-spin correlation functions defined as

$$\mathcal{S}_{ij} = \langle \hat{S}_i \cdot \hat{S}_j \rangle = \left\langle \frac{1}{2} (\hat{S}_i^+ \hat{S}_j^- + \hat{S}_i^- \hat{S}_j^+) + \hat{S}_i^z \hat{S}_j^z \right\rangle, \quad (7)$$

where \hat{S}_i^\pm is spin rising(lowering) operator. First, we analyze the expectation value of the squared spin operator $\langle \hat{S}_\alpha^2 \rangle \equiv \mathcal{S}_{i(\alpha)i(\alpha)}$ on each sublattice α as shown in Fig. 9. It is clearly visible that the enhancement of V resulting in the formation of (100) ordering also affects the magnetic properties. Although for the lower values of the intersite interactions, the quantity $\langle \hat{S}_\alpha^2 \rangle$ is almost constant with the value ~ 0.5 for each α , the development of CDW intensifies the asymmetry with respect to the sublattices. When the gap opens and $V \gtrsim 3.5|t|$, both $\langle \hat{S}_A^2 \rangle$ and $\langle \hat{S}_B^2 \rangle$ ³³ reach a value close to 3/4, indicating spin localization at sites assigned to the occupied sublattices. Eventually, when the (200) ordering appears, the mean value of the squared spin operator only slightly exceeds the value of 0.1, indicating that the doubly occupied sublattice sites C refer to isolated on-site singlets.

Subsequently, we focus on the detailed analysis of the spin properties of (110) GWC in the range $5.5|t| \gtrsim V \gtrsim 3.5|t|$. To reduce the bias coming from the open boundary conditions along \mathbf{R}_1 we set i referring to the site being in the vicinity of $L_1/2$ and change j as shown in Fig. 10, where we plot \mathcal{S}_{ij} for the three representative values of V ($3.5|t|$, $4.5|t|$ and $5.5|t|$).

As one can see from Fig. 10 (a) and (b) a well pronounced antiferromagnetic order can be identified in the GWC state for the lower values of V (but already within the ((110) state), since the characteristic oscillations of sign in the correlation functions corresponding to the occupied sites (A and B) appear. As expected, when we set i belonging to A sublattice and j belonging to the almost empty sublattice C, we obtain $\mathcal{S}_{ij} \approx 0$ (cf. Fig. 5) for

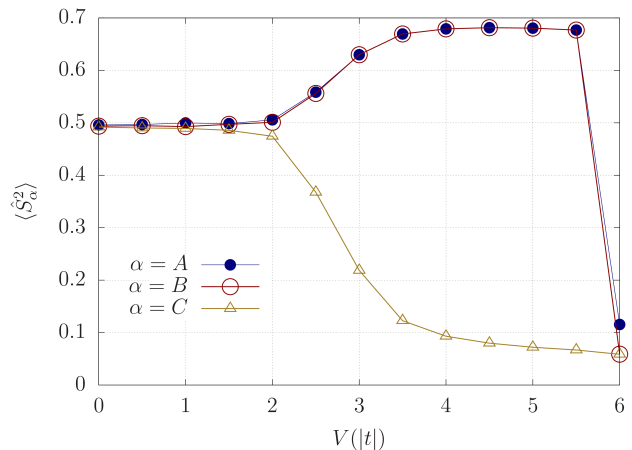


FIG. 9. Expectation value of the \hat{S}^2 operator per lattice site as a function of inter-site Coulomb repulsion amplitude V .

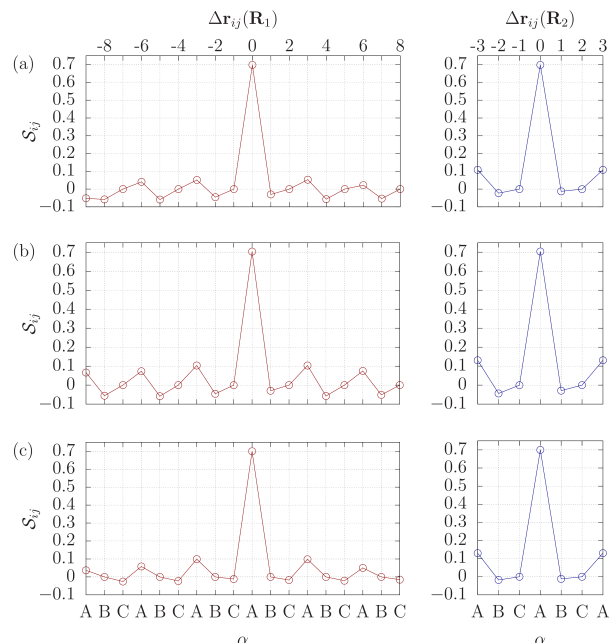


FIG. 10. Spin-spin correlation functions \mathcal{S}_{ij} obtained for 24×6 supercell for $V = 3.5|t|$ (a), $V = 4.5|t|$ (b) and $V = 5.5|t|$ (c). The left panel refers to the \mathbf{R}_1 direction, whereas the right panel refers to the \mathbf{R}_2 direction. Note, that range is truncated since we intend to set i -index at site referring to A sublattice for each considered value of intersite interaction amplitude V .

$V < 5|t|$. However, when $V \gtrsim 5|t|$ the correlation functions between two occupied sites are strongly suppressed ($\mathcal{S}_{AB} \approx 0$) regardless of the distance between the two lattice sites (cf. Fig. 10c). This indicates that in this regime of long-range Coulomb repulsion strength V , we no longer have a standard antiferromagnetic ordering.

To gain deeper insight into the character of magnetic ordering in the considered system we calculate the out-of-plane and in-plane components of the spin-spin corre-

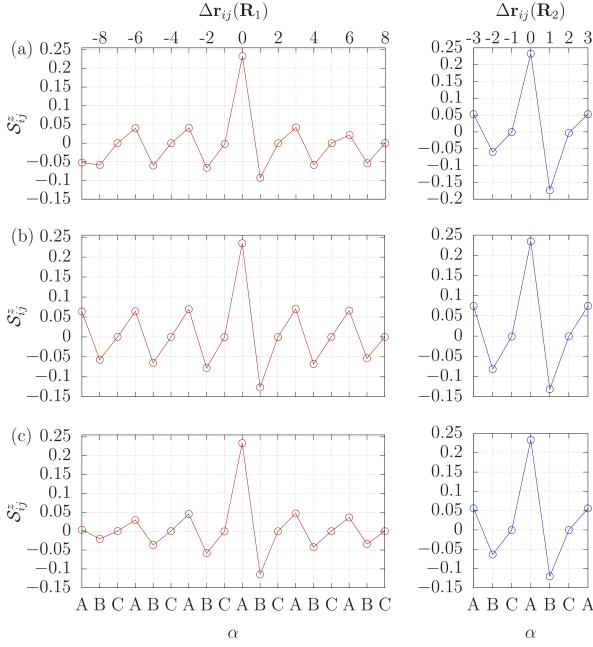


FIG. 11. The correlation functions corresponding to the z component of spin for the three representative values of V , that is: $V = 3.5|t|$ (a), $V = 4.5|t|$ (b), and $V = 5.5|t|$ (c) similarly as in Fig.10.

lation functions, i.e.,

$$\mathcal{S}_{ij}^z = \langle \hat{S}_i^z \hat{S}_j^z \rangle, \quad (8)$$

and

$$\mathcal{S}_{ij}^{xy} = \left\langle \frac{\hat{S}_i^+ \hat{S}_j^- + \hat{S}_i^- \hat{S}_j^+}{2} \right\rangle, \quad (9)$$

respectively. In Fig. 11, we present the spatial dependence of \mathcal{S}_{ij}^z analogously to Fig. 10. We observe that up to $V \approx 5|t|$ the antiferromagnetic pattern is robust for the z -th component of spin. As can be seen, the absolute value of \mathcal{S}_{ij}^z is characterized by a very weak spatial decay. For $V \gtrsim 5|t|$ the maximal amplitude is noticeably smaller and distinctly decays with increasing distance between occupied lattice sites; however, the sign clearly oscillates indicating a tendency towards out-of-plane antiferromagnetic order

According to the evidence given above, the relation $\mathcal{S}_{AB} \approx 0$ that holds only for neighboring sites when $V \lesssim 5|t|$ and is independent of the spatial separation for $V \gtrsim 5|t|$ needs to originate from the in-plane components \mathcal{S}_{AB}^{xy} of the spin-spin correlation function. Therefore, to complete our analysis, we present \mathcal{S}_{AB}^{xy} in Fig. 12. The general observation is that higher values of V (but in the range of V that reproduce the stability of GWC (110)) result in a substantially weaker spatial decay in \mathcal{S}_{ij}^{xy} . Furthermore, the maximal amplitude increases with increasing V . We identify this behavior as an indicator of a tendency towards spin *canting*. The enhancement in

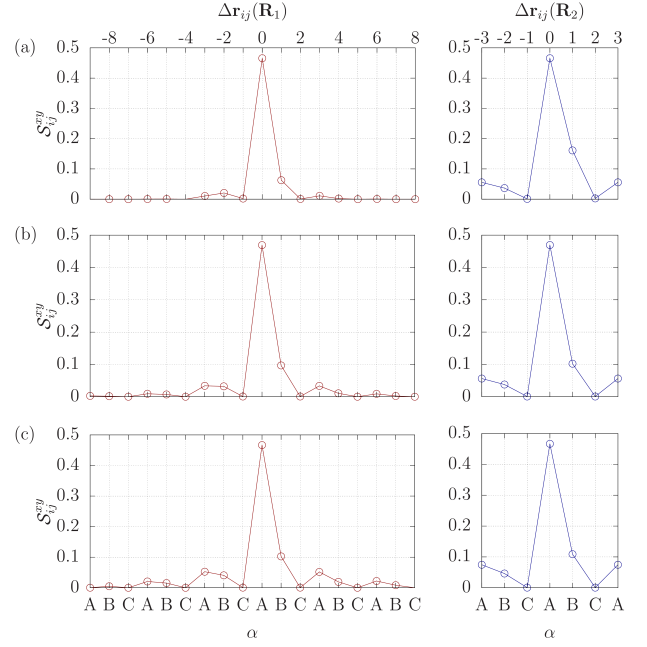


FIG. 12. The $x - y$ spin-spin correlation function for the selected values of V , that is: $V = 3.5|t|$ (a), $V = 4.5|t|$ (b), and $V = 5.5|t|$ (c) similarly as in Figs. 10,11. The increase in both the magnitude and spatial extension is clearly visible when V approaches range for which system becomes close to (200) phase.

both the amplitude and spatial range of in-plane correlations with the simultaneous attenuation of antiferromagnetic order results in an extreme form of *canting* between neighboring spins for $V \gtrsim 5|t|$, that is, they become almost perpendicular to each other since $\mathcal{S}_{AB}^{xy} \approx -\mathcal{S}_{AB}^z \neq 0$ holds.

Our findings based on the analysis carried out in the real space are compactly presented in Fig.13 where we present both \mathcal{S}_{AB}^z and \mathcal{S}_{AB}^{xy} as functions of V in the range where the (110) phase has been confirmed. In the main plot, we consider the case where the sublattice sites A and B are separated by $\Delta \mathbf{r}_{ij} = 7\Delta \mathbf{R}_1$, that is, the range for which the result is still not affected by the open boundary conditions. It is clearly visible that spin-spin correlations related to $x - y$ plane start to participate in the overall spin properties mainly when $V \gtrsim 4.5|t|$. Below this value, they *affect* \mathcal{S}_{AB} in the very limited spatial range. However, a coincident decrease in the absolute value of \mathcal{S}_z with increasing V results in the perpendicular pattern between spins residing in the occupied sublattices A and B .

For the sake of completeness we have carried out a complementary analysis in the reciprocal space, which provides indicators of the described effects taking into account the whole volume of the supercell. Namely, we

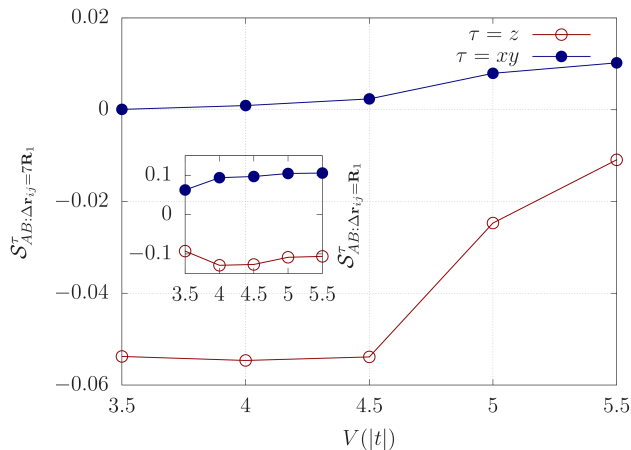


FIG. 13. The resultant \mathcal{S}_{AB}^z and \mathcal{S}_{AB}^{xy} for (110) phase as a function of V collected for $\Delta\mathbf{r}_{ij} = 7\Delta\mathbf{R}_1$ (main plot) and for $\Delta\mathbf{r}_{ij} = \Delta\mathbf{R}_1$ (inset).

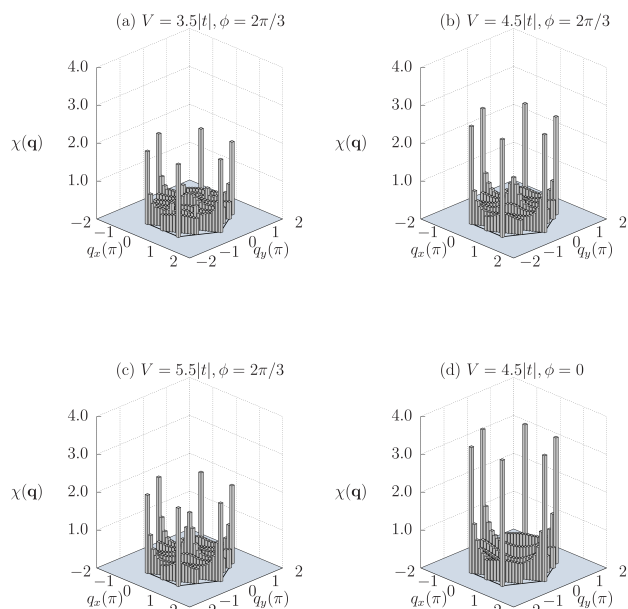


FIG. 14. Spin structure factor $\chi(\mathbf{q})$ obtained for the three representative values of V with spin-valley polarization effectively induced by putting phase $\phi = 2\pi/3$ in the non-interacting (single particle) part of Hamiltonian (see Eq. 1) (a)-(c); $\chi(\mathbf{q})$ obtained for $V = 4.5|t|$ and $\phi = 0$ (cf. (b)).

have investigated the spin structure factor defined as

$$\chi(\mathbf{q}) = \sum_{i,j} e^{i\mathbf{q}\cdot(\mathbf{r}_i - \mathbf{r}_j)} \mathcal{S}_{ij}, \quad (10)$$

for \mathbf{q} points presented Fig. 6.

The dominant tendency towards antiferromagnetic order is clearly reflected in the landscape of $\chi(\mathbf{q})$ by the presence of peaks located at \mathbf{K} and \mathbf{K}' points as shown

in Fig. 14(a-c). However, with increasing value of V we observe pronounced development of a peak located at Γ which suggests the formation of a ferromagnetic order. This behavior can be fully understood in terms of the reasoning carried out in the real space. Namely, the spin canting is enhanced with increasing magnitude of V in (110) GWC state resulting in *mixture* of two kind of orders: antiferromagnetic and ferromagnetic. We identify this effect as resulting from the presence of spin-valley polarization in the system since we do not observe the peak for $\chi(\Gamma)$ when we set the phase $\phi = 0$ (see Fig. 14d) in the auxiliary calculations performed for $V = 4.5|t|$ for the same system size and the maximal link dimension. The $\phi = 0$ situation leads to the absence of the spin-valley locking meaning that one deals with a single doubly degenerate band.

IV. SUMMARY

In this paper, we have analyzed the minimal model of WSe_2/WS_2 heterobilayer at fractional filling $2/3$ for which the existence of a generalized Wigner crystal has been experimentally reported. Our approach is based on the extended Hubbard Hamiltonian on a triangular lattice, and the nearest-neighbor Coulomb repulsion V has been treated as a free parameter. Essentially, the non-interacting (single-particle) part of the Hamiltonian has been equipped with complex-valued hopping amplitudes, reproducing the spin-valley splitting which is an inherent feature of this system. The Density Matrix Renormalization group method has been utilized for finding the approximate ground state and its electronic properties.

By setting the on-site Hubbard interaction $U = 15|t|$ and the intersite repulsion in the range $5.5|t| \gtrsim V \gtrsim 3|t|$, we were able to reproduce the formation of a generalized Wigner crystal, which is characterized by the (110) sublattice occupation scheme. Namely, the occupied (empty) sites form a honeycomb (triangular) lattice in such a charge pattern. Furthermore, in addition to analyzing the properties of single particles both in real space and momentum, we provide direct evidence of the insulating character of the (110) phase by inspecting charge-charge correlation functions resolved with the Fourier transform at small wave numbers.

Subsequently, we have carried out the analysis of spin properties of the system by studying the spatial behavior of the in- and out-of-plane spin-spin correlation functions separately. Our investigation revealed that in the range of parameters V for which a honeycomb charge pattern appears in the underlying triangular lattice, the strong tendency towards the formation of antiferromagnetic ordering becomes reduced with increasing value V with a concomitant development of spin-canting. We have observed the extreme form of this *canting* for the maximal values of V for which the charge order (110) is stable. In such a situation, the neighboring spins in the honeycomb lattice tend to be perpendicular to each other. This ob-

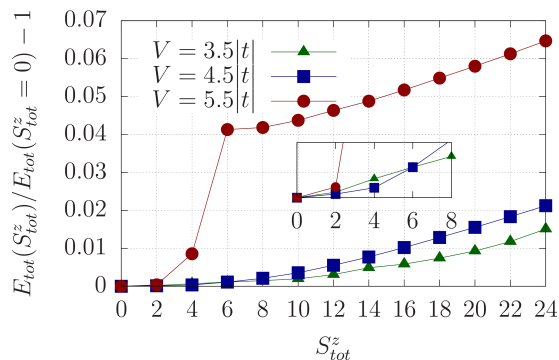


FIG. A1. The total energy per lattice site of the $L_1 \times L_2 = 12 \times 6$ supercell at filling $2/3$ for the three values of V representative for (110) GWC examined in details. The lowest energy is obtained for $S_{tot}^z = 0$ for each considered V .

servation indicates that at least at high values of V the generalized Wigner crystal should gain a nonzero total magnetization.

In view of the results obtained here, it can be expected that the magnetic properties of the emerging generalized Wigner crystal in WSe_2/WS_2 can change with modifications of the experimental setup, such as substrate modifications¹⁶, which impact the dielectric function and in turn can change the relative balance between V , U , and W . We hope to see experimental evidence in this regard soon, as well as experimental evidence concerning

spin order in these fascinating systems³⁴.

ACKNOWLEDGMENTS

This research was funded by National Science Centre, Poland (NCN) according to decision 2021/42/E/ST3/00128. For the purpose of Open Access, the author has applied a CC-BY public copyright licence to any Author Accepted Manuscript (AAM) version arising from this submission.

We gratefully acknowledge Poland's high-performance Infrastructure PLGrid ACK Cyfronet AGH for providing computer facilities and support within computational grant no. PLG/2024/017227.

Appendix: $S_z^{tot} = 0$ assumption

To investigate if the $S_z^{tot} = 0$ assumption biases our predictions, we performed the set of additional calculations for the supercell of size $L_1 \times L_2 = 12 \times 6$. We have selected the intersite repulsions $V = \{3.5|t|, 4.5|t|, 5.5|t|\}$ as a representative for the characterization of (110) GWC. We examined the cases for which $S_{tot}^z = \{0, 2, 4, \dots, 24\}$. Note that $S_{tot}^z = 24$ refers to the fully polarized system at filling $2/3$ for a cluster of this size. As one can see in Fig. A1 the minimum of the total energy E_{tot} corresponds to the case where $S_{tot}^z = 0$ in all three cases. Therefore, we find that the assumption $S_z^{tot} = 0$ in the simulations is justified.

* andrzej.biborski@agh.edu.pl

† michal.zegrodnik@agh.edu.pl

¹ M. Imada, A. Fujimori, and Y. Tokura, *Rev. Mod. Phys.* **70**, 1039 (1998).

² Y. Cao, V. Fatemi, A. Demir, S. Fang, S. L. Tomarken, J. Y. Luo, J. D. Sanchez-Yamagishi, K. Watanabe, T. Taniguchi, E. Kaxiras, R. C. Ashoori, and P. Jarillo-Herrero, *Nature* **556**, 80 (2018).

³ B. Keimer, S. A. Kivelson, M. R. Norman, S. Uchida, and J. Zaanen, *Nature* **518**, 179 (2015).

⁴ Y. Cao, V. Fatemi, S. Fang, K. Watanabe, T. Taniguchi, E. Kaxiras, and P. Jarillo-Herrero, *Nature* **556**, 43 (2018).

⁵ E. Wigner, *Phys. Rev.* **46**, 1002 (1934).

⁶ M. Chiao, *Nature Reviews Physics* **6**, 348 (2024).

⁷ Y.-C. Tsui, M. He, Y. Hu, E. Lake, T. Wang, K. Watanabe, T. Taniguchi, M. P. Zaletel, and A. Yazdani, *Nature* **628**, 287 (2024).

⁸ E. C. Regan, D. Wang, C. Jin, M. I. Bakti Utama, B. Gao, X. Wei, S. Zhao, W. Zhao, Z. Zhang, K. Yumigeta, M. Blei, J. D. Carlström, K. Watanabe, T. Taniguchi, S. Tongay, M. Crommie, A. Zettl, and F. Wang, *Nature* **579**, 359 (2020).

⁹ Y. Xu, S. Liu, D. A. Rhodes, K. Watanabe, T. Taniguchi, J. Hone, V. Elser, K. F. Mak, and J. Shan, *Nature* **587**,

214 (2020).

¹⁰ X. Huang, T. Wang, S. Miao, C. Wang, Z. Li, Z. Lian, T. Taniguchi, K. Watanabe, S. Okamoto, D. Xiao, S.-F. Shi, and Y.-T. Cui, *Nature Physics* **17**, 715 (2021).

¹¹ H. Li, S. Li, E. C. Regan, D. Wang, W. Zhao, S. Kahn, K. Yumigeta, M. Blei, T. Taniguchi, K. Watanabe, S. Tongay, A. Zettl, M. F. Crommie, and F. Wang, *Nature* **597**, 650 (2021).

¹² H. Zhou, K. Liang, L. Bi, Y. Shi, Z. Wang, and S. Li, *ACS Applied Electronic Materials* **6**, 1530 (2024).

¹³ L. Rademaker, *Phys. Rev. B* **105**, 195428 (2022).

¹⁴ Y. Tan, P. K. H. Tsang, V. Dobrosavljević, and L. Rademaker, *Phys. Rev. Res.* **5**, 043190 (2023).

¹⁵ J. Motruk, D. Rossi, D. A. Abanin, and L. Rademaker, *Phys. Rev. Res.* **5**, L022049 (2023).

¹⁶ N. Morales-Durán, P. Potasz, and A. H. MacDonald, *Phys. Rev. B* **107**, 235131 (2023).

¹⁷ S. F. Ung, J. Lee, and D. R. Reichman, *Phys. Rev. B* **108**, 245113 (2023).

¹⁸ A. Amaricci, A. Camjayi, K. Haule, G. Kotliar, D. Tanasković, and V. Dobrosavljević, *Phys. Rev. B* **82**, 155102 (2010).

¹⁹ S. R. White, *Phys. Rev. Lett.* **69**, 2863 (1992).

- ²⁰ U. Schollwöck, *Annals of Physics* **326**, 96 (2011), january 2011 Special Issue.
- ²¹ G. Catarina and B. Murta, *The European Physical Journal B* **96**, 111 (2023).
- ²² M. Fishman, S. R. White, and E. M. Stoudenmire, *SciPost Phys. Codebases*, 4 (2022).
- ²³ T. Shirakawa, T. Tohyama, J. Kokalj, S. Sota, and S. Yunoki, *Phys. Rev. B* **96**, 205130 (2017).
- ²⁴ A. Szasz, J. Motruk, M. P. Zaletel, and J. E. Moore, *Phys. Rev. X* **10**, 021042 (2020).
- ²⁵ A. Szasz and J. Motruk, *Phys. Rev. B* **103**, 235132 (2021).
- ²⁶ L. F. Tocchio, C. Gros, X.-F. Zhang, and S. Eggert, *Phys. Rev. Lett.* **113**, 246405 (2014).
- ²⁷ A. Biborski, (2024), 10.5281/zenodo.13380604.
- ²⁸ J. Spałek, M. Fidrysiak, M. Zegrodnik, and A. Biborski, *Physics Reports* **959**, 1 (2022).
- ²⁹ M. Capello, F. Becca, M. Fabrizio, S. Sorella, and E. Tosatti, *Phys. Rev. Lett.* **94**, 026406 (2005).
- ³⁰ L. F. Tocchio, F. Becca, and C. Gros, *Phys. Rev. B* **83**, 195138 (2011).
- ³¹ L. F. Tocchio, A. Montorsi, and F. Becca, *Phys. Rev. B* **102**, 115150 (2020).
- ³² A. Biborski, P. Wójcik, and M. Zegrodnik, *Phys. Rev. B* **109**, 125144 (2024).
- ³³ We omit the lattice site index where it can be considered as redundant in this particular context.
- ³⁴ F. Pichler, W. Kadow, C. Kuhlenkamp, and M. Knap, *Phys. Rev. B* **110**, 045116 (2024).